ARTICLE

Chiral Plasmonic Nanowaves by Tilted Assembly of Unidirectionally Aligned Block Copolymers with Buckling-Induced Microwrinkles

Junghyun Cho,[#] Myonghoo Hwang,[#] Minkyung Shin,[#] Jinwoo Oh, Jinhan Cho, Jeong Gon Son,* and Bongjun Yeom*

| ACCESS | 📊 Metrics & More | 📰 Article Recommendations | 🆘 Supporting Information |

ABSTRACT: Chiral-structured nanoscale materials exhibit chiroptical properties with preferential absorptions of circularly polarized light. The distinctive optical responses of chiral materials have great potential for advanced optical and biomedical applications. However, the fabrication of three-dimensional structures with mirrored nanoscale geometry is still challenging. This study introduces chiral plasmonic nanopatterns in wavy shapes based on the unidirectional alignment of block copolymer thin films and their tilted transfer, combined with buckling processes. The cylindrical nanodomains of polystyrene-*block*-poly(2-vinylpyridine) thin films were unidirectionally aligned over a large area by the shear-rolling process. The aligned block copolymer thin films were transferred onto uniaxially prestrained polydimethylsiloxane films at certain angles relative to the stretching directions. The strain was then released to induce buckling. The aligned nanopatterns across the axis of the formed microwrinkles were selectively infiltrated with gold ions. After reduction by plasma treatment, chiral plasmonic nanowave patterns were fabricated with the presence of mirror-reflected circular dichroism spectra. This fabrication method does not require any lithography processing or innately chiral biomaterials, which can be advantageous over other conventional fabrication methods for artificial nanoscale chiral materials.

KEYWORDS: chirality, block copolymer, buckling, microwrinkle, transfer, alignment, circular dichroism
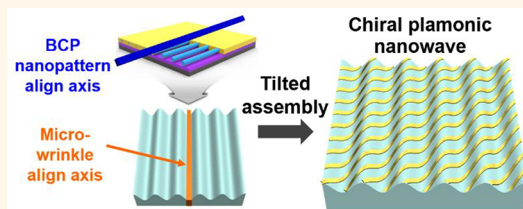
Recent advances in the field of chiral nanomaterials have drawn great attention because of the distinctive chiroptical properties of such nanomaterials[1,2] and their potential applications in advanced optical and biomedical devices, such as metamaterials,[3,4] holographic displays,[5] chiroptical field separations,[6,7] and biosensor platforms.[8,9] Nanostructured materials with chiral geometries can preferentially interact with circularly polarized light in specific wavelength ranges that are mainly attributed to the electronic transitions, charge transfer, and plasmonic absorptions of the constituent materials. The three-dimensional shapes of chiral structures significantly affect the appearance and magnitude of chiroptical responses.

For the fabrication of artificial chiral nanomaterials, various approaches have been reported, such as chiral ligand-directed synthesis,[10,11] e-beam lithography,[12,13] DNA origami self-assembly,[14,15] and 3D kirigami assembly with nano- and microsized cut patterns.[16,17] However, there are major concerns regarding the high cost of equipment and processes and the low stability of innate biomaterials and DNA under

harsh environments, which weaken their potential for broader applications. Mass production is also limited owing to their low processabilities. Recently "lithography- and biomaterial-free" methods were reported for the fabrication of chiral geometries at the nano- and microscale. Clockwise or counterclockwise rotations of nanotemplate substrates with inclined vapor depositions yielded chiral nanohelices[18,19] and plasmonic nanoshells.[20,21] Asymmetric mechanical stresses on flexible substrates were also utilized to align plasmonic nanoparticles into S-like chains[22] and fusilli-pasta-shaped microsized patterns.[23] However, delicate control of the alignment of nanoscale objects remains difficult to achieve without the aid
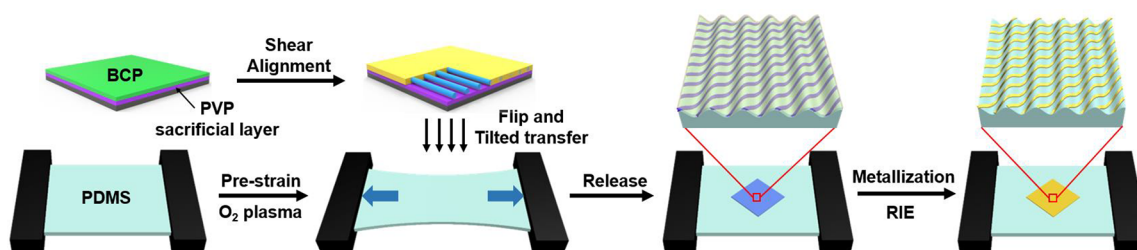
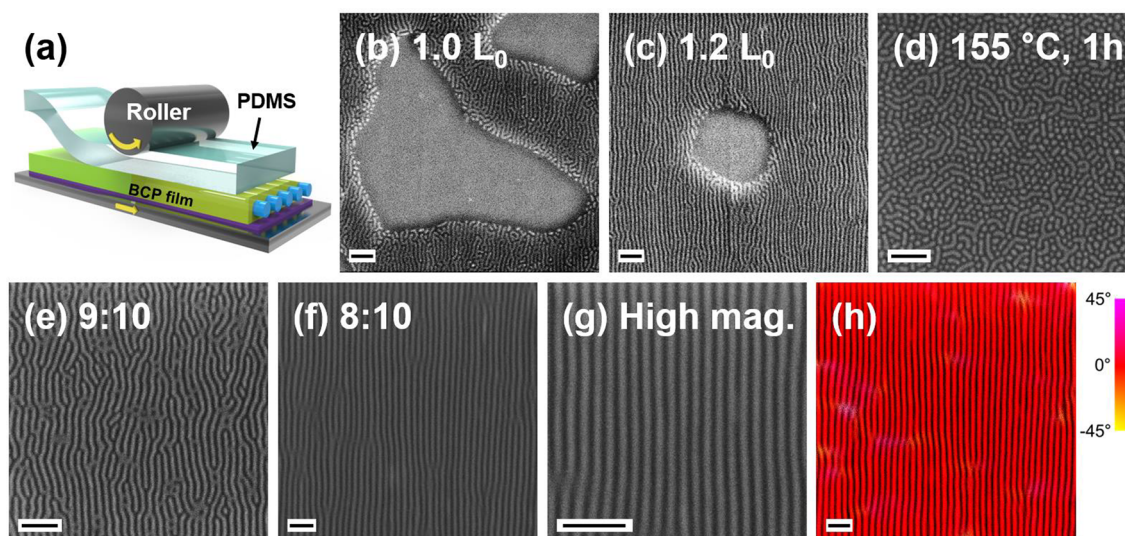Figure 1. Schematic of the fabrication process of the chiral plasmonic nanowave patterns.

Figure 2. (a) Schematic of shear-rolling process. (b,c) SEM images of the PS-*b*-P2VP films on PVP sacrificial layers with different BCP film thicknesses of (b) 38 nm (~1 L_0), (c) 46 nm (~1.2 L_0), and (d–h) 58 nm (~1.5 L_0). (d) Films with only thermal annealing at 155 °C for 1 h. (e,f) SEM images of shear-rolled films with different ratios of stage/roller speeds of (e) 9:10 and (f) 8:10. (g) High magnification image of image f. (h) Orientation order map of image f. Scale bars indicate 200 nm.

of highly advanced lithography techniques, such as focused ion beam[24] and e-beam lithography.

Block copolymer (BCP) thin films and their self-assembly behaviors with phase-separated nanodomains have been examined for their potential applications in advanced optical and electronic devices, such as next-generation lithography,[25] high-density data storage,[26] photonic crystals, and metamaterials.[27] For device fabrication, the alignment of BCP nanodomains over large areas is essential; however, randomly oriented patterns such as fingerprinting are usually formed because of the nature of self-assembly. Therefore, several methods, such as graphoepitaxy,[28] chemoepitaxy,[29,30] and shear alignment,[31,32] for directed self-assembly that guide the BCP nanodomains into desired layouts have been studied. Recently, we reported a shear-rolling process capable of the unidirectional alignment of BCP nanodomains on the Si wafer scale in 1 min.[33] By performing hot rolling with different speeds between the stage and roller, a large shear was sequentially applied to the BCP thin film as a big wave, enabling the successful unidirectional alignment of nanodomains with an orientation order of 0.98 at a very high speed over a large area.

Cross-finger or scissor-type alignments of two anisotropic objects are among of the simplest chiral shapes.[34−37] For example, if two individual aligned objects are stacked laterally with a tilting angle, similar to crossed fingers with left- or right-handedness, the assembled structure has mirror symmetry and its chirality is determined by the tilting angle between the two aligned objects. Chiral graphene bilayer films prepared by the stacking approach presented preferred absorptions of circularly polarized lights with tunable optical bands.[34] DNA origami methods were utilized to fabricate tilted assembly of plasmonic nanorods in cross-fingered geometries.[35,36] Recently, cross-stacked nanoparticle chain arrays showed mechanically tunable chiroptical responses in the vis-NIR region.[37] Laser interference lithography is required to prepare nanochannel master patterns for the anisotropic assembly of the nanoparticle chains. Thus, it is still challenging to fabricate artificial chiral nanomaterials without assists of any lithography methods or bioderived materials.

In this study, based on the design motif of crossed fingers, the unidirectionally aligned nanodomains of BCP thin films and uniaxial microwrinkles formed by buckling served as the anisotropic objects. The cylindrical nanodomains of polystyrene-*block*-poly(2-vinylpyridine) (PS-*b*-P2VP) thin films were unidirectionally aligned in a large area with assistance by our shear-rolling process. The aligned BCP films were then transferred to the surfaces of uniaxially prestrained polydimethylsiloxane (PDMS) substrates at tilted angles relative to the stretching direction. The release of the prestrain induced regular microwrinkle structures perpendicular to the strain direction, and the resultant structures had chiral nanowave patterns in which aligned nanodomains lay across the axis of the microwrinkles in oblique directions. These asymmetrically aligned nanopatterns have chirality due to lacks of an improper (S_n) axis of symmetry (a mirror plane, $\sigma = S_1$, a center of
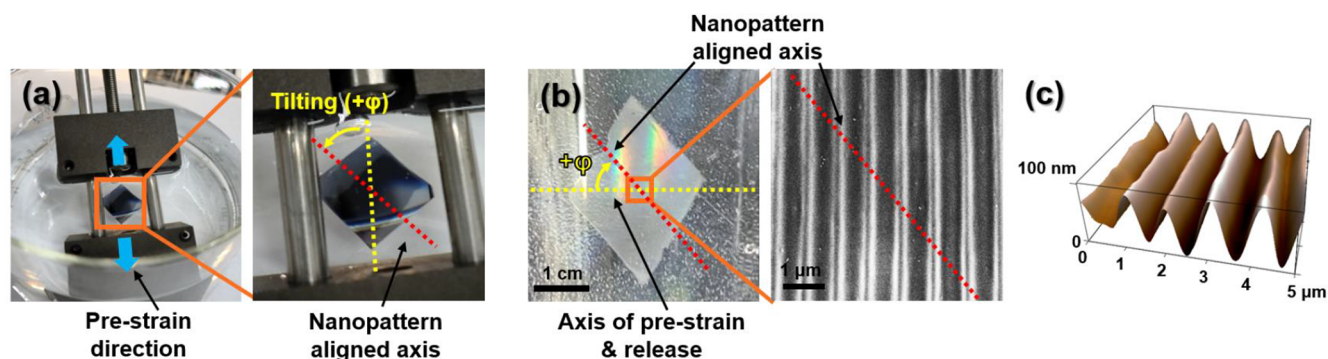
Figure 3. (a) Photographic images of BCP pattern transfer process onto the prestained PDMS substrate. The PDMS substrate with the attached BCP film on the wafer is placed upside-down in water. (b) Transferred BCP film on the released PDMS substrate. Representative SEM plane image is shown of the film with the tilt angle (φ) of +45°. (c) AFM image of unidirectionally formed microwrinkled structure from the surface instability of the BCP thin film on the 30% prestrained PDMS after the strain release process.

inversion, $i = S_2$, and a rotation-reflection axis, S_n) (Figure S1). To impart plasmonic responses to the chiral nanopatterns, we performed liquid-phase infiltration (LPI) of a gold solution to selectively transform the cylindrical nanodomains into gold particle arrays in wave shapes.[38,39] Mirror-shaped chiroptical responses were observed for the chiral plasmonic nanowave patterns with the tilt angles of 45° and −45°. The work described in this paper is achieved by an attractive combination of two different self-assembly processes, the directed assembly of BCP thin films and buckling-induced microwrinkles, for the facile fabrication of chiral plasmonic nanomaterials. It would serve as a simple and valuable example of a "lithography- and biomaterial-free" fabrication strategy, and thus may be advantageous relative to other approaches for large area production of the artificial chiral materials.

RESULTS AND DISCUSSION

Figure 1 shows the fabrication process for the chiral plasmonic nanowave patterns. First, a 1 wt % polyvinylpyrrolidone (PVP) aqueous solution was spin-coated at 6000 rpm on UV−ozone-cleaned Si wafers to a thickness of ∼20 nm. PVP has a glass transition temperature of approximately 170 °C, allowing stable maintenance of the layer during the shear-rolling process. PVP is also water-soluble and is chosen as a sacrificial layer to transfer the BCP film onto the PDMS substrate. Subsequently, a solution of 1.7 wt % of PS-*b*-P2VP with asymmetric molecular weights of 44−18.5 kg·mol^{-1} in toluene was spin-coated onto the PVP-coated Si wafer. The BCP spontaneously formed cylindrical nanodomains with a 39.2 nm period through nanophase separation after heat treatment. However, in general, the self-assembly of the BCP yields randomly oriented fingerprinting patterns.

The shear-rolling process was performed for the unidirectional orientation of the cylinders. Figure 2a shows a schematic of the shear-rolling process inducing unidirectional alignment of the BCP film. The speed of the roller and the stage was varied after attaching a 0.8 mm-thick PDMS pad to the film to allow even application of shear to the film during hot rolling. Because the typical static shear method evenly applies pressure and shear stress to the entire area of the sample, the pressure and shear force must increase in proportion to the size of the sample. In addition, a relatively longer fabrication time is required. These could be drawbacks for large-area fabrication and mass production. However, in our shear-rolling process, shear is sequentially applied to a localized area in less than 1 s,

offering the advantage of quick repetitive shearing even over large sample sizes reaching the wafer level. Shear rolling was performed at 155 °C with films of various thicknesses to determine the optimal conditions for obtaining highly aligned parallel cylindrical nanodomains, as shown in Figure 2b−f. During thermal annealing, terrace structures (holes or islands) were formed to follow the commensurability between the domain spacing (L_0) of the BCP and the film thickness; these caused unwanted polymer flow and surface roughness.[40] The PS-*b*-P2VP film has an asymmetric wetting condition in our experimental setup, in which the P2VP domain is wetted at the bottom in contact with the PVP and the PS domain is wetted on the top in contact with the PDMS. Therefore, the flat surface of the BCP film can be maintained only when the film has a half-integer thickness of L_0. Therefore, the shear-rolled BCP film with a thickness near 1 L_0 (∼38 nm) in Figure 2b shows a terrace structure with partially aligned cylinders. The film of 1.2 L_0 thickness in Figure 2c shows cylinders oriented to some extent; however, vacant places appear in several locations. At 1.5 L_0 thickness (∼58 nm), the film shows monolayers of cylinders that are highly aligned in one direction without vacancies or major vortices. This commensurability-related result cannot be seen in conventional static shearing, where shear is applied simultaneously across the entire surface.[41]

Next, we examined the degree of alignment of the cylindrical BCP nanodomains under various shear conditions by adjusting the roller and stage speeds individually. For the control experiment, the PS-*b*-P2VP films after thermal annealing at 155 °C for 1 h without applying shear showed typical randomly oriented fingerprinting patterns (Figure 2d). The repetitively shear-rolled BCP film (back-and-forth five times) with a stage speed of 9 mm·s^{-1} and a roller speed of 10 mm·s^{-1} (shear rate = 1.25 s^{-1}, Figure 2e) exhibited relatively less oriented cylindrical patterns, indicating that insufficient shear leads to less alignment of the BCP nanodomains in thin films. Under the relatively stronger shear conditions of 8:10 (shear rate = 2.5 s^{-1}, Figure 2f,g), highly aligned cylindrical patterns in the shear direction could be obtained. The aligned pattern period is ∼40.4 nm which is slightly larger than the nonsheared pattern (∼39.2 nm) in Figure 2d, which is a common phenomenon as shearing causes the BCP chains to elongate in the vertical direction of shear. We quantified the orientation of the BCP nanodomains based on the orientation order parameter obtained from image analysis and the equation Ψ
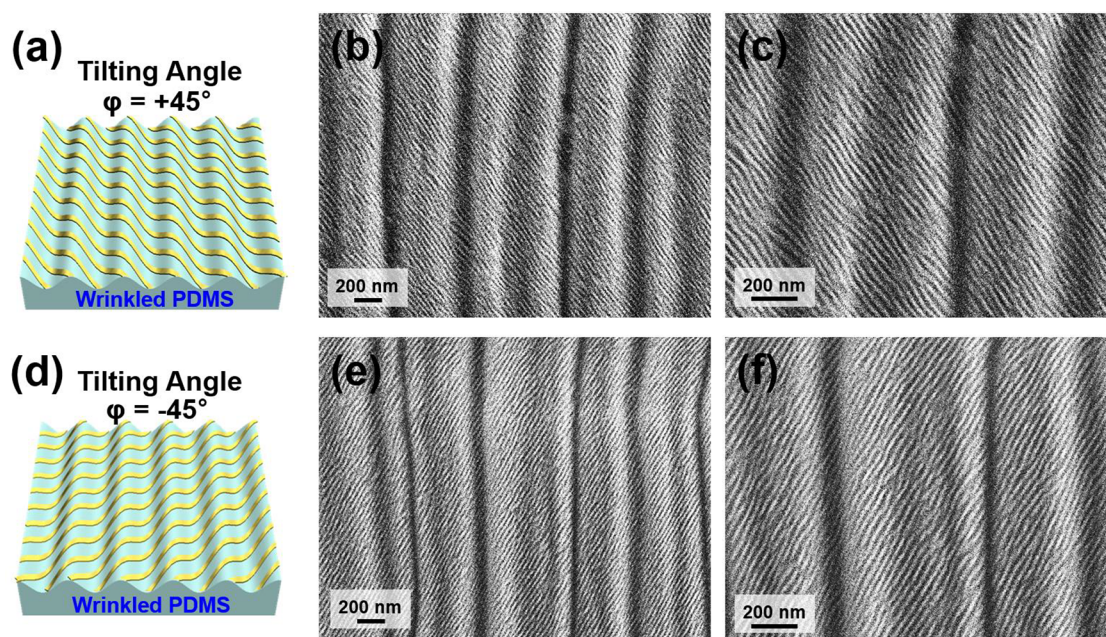
Figure 4. Schematics and SEM images of BCP aligned nanopatterns metallized with gold transferred onto unidirectional microwrinkle patterns with different tilt angles (φ) of (a–c) +45° (d–f) −45°. SEM images from left to right are arranged from low to high magnifications.

= $\langle \cos[2(\theta - \theta_0)] \rangle$, where Ψ is the orientation order parameter, θ is the local orientation of the line, and θ_0 is the direction of shear. In most well-oriented images, high degrees of orientation over 0.97 were obtained. The orientational order map shown in Figure 2h obtained by image analysis of Figure 2h showed a high degree of orientation of 0.985.

Subsequently, the unidirectionally aligned BCP patterns were transferred to the prestrained PDMS substrate (Figure 1). After preparing the fully cured 1 mm-thick transparent PDMS substrate, it was mounted on the jigs of a device for prestrain application, uniaxially stretched to a strain of 30%, and treated with oxygen plasma (150 W, 20 sccm, 20 mTorr, 10 s) to improve the adhesion between the BCP film and PDMS to form hard silicate layer for the stable wrinkle structure. The BCP films on the Si wafer were attached to the prestrained PDMS at specific tilt angles, and then immersed up-side down in water, as shown in Figure 3a. Clockwise tilting is denoted by positive tilt angles from the axis of the prestrain direction, such as the tilt angle φ of +45° in Figure 3a,b. Counterclockwise tilting is denoted by a negative tilt angle. The PVP sacrificial layer was dissolved in warm water at 60 °C, and the BCP films were spontaneously transferred from the wafer to the PDMS substrates over several minutes. After the transfer, the exposed P2VP cover layer and PS thin layer on the surface were etched with Ar plasma (150 W, 20 sccm, 30 s, 25 nm etched), and then the prestrain was released. Ar plasma treatment was introduced to remove the overlaid polymeric layer that can deteriorate the selective and uniform metallization at the P2VP cylindrical domains for the last metal infiltration process. It was confirmed that the transferred square-shaped BCP film shrank into a rhombus shape. Multiple colors appeared because of the formation of microwrinkles on the surface, as shown in Figure 3b.

Figures 3b,c show the scanning electron microscopy (SEM) and atomic force microscopy (AFM) images of the microwrinkles formed after the BCP film transfer and prestrain release. During the release of the prestrain, a compressive strain was applied to the relatively hard BCP film, and

microwrinkles were formed with an alignment perpendicular to the prestrain direction. The unidirectional microwrinkles form periodic oscillatory micropatterns with a periodicity of ∼900 nm and an amplitude of ∼50 nm. We also observed nanoscale wrinkles (∼250 nm period in Figure S2) even in the nontransferred regions of PDMS due to the hard silicate layer formed by the O_2 plasma. The period of the wrinkle structure follows the formula related to the moduli of the substrate (E_s, PDMS ∼ 1.5 MPa) and the surface film (E_f, PS-b-P2VP ∼ 4.2 GPa[42] and silicate layer) and the thickness of the surface film (h), $\lambda \sim 2\pi h(E_f/3E_s)^{1/3}$. The amplitude relates the applied compressive strain (ε) to the above.[43] $A \sim h\sqrt{4\varepsilon(E_f/3E_s)^{2/3} - 1}$. Large stress is mainly concentrated at the interface between the hardest silicate and the PDMS formed gradually through plasma, and the transferred BCP film with a modulus between silicate and PDMS is relatively less stressed and serves to add the thickness of the hard surface layer. This causes wrinkles with BCP films to form a wider period of wrinkles than the nontransferred region of the PDMS. In addition, the mechanical properties of the surface film (E_f and h) are changed through the metallization process immersed in a strong acid solution and the O_2 plasma process to remove the residual BCP polymers, so the wrinkle period also changes accordingly.

The cylindrical domains of the wrinkled BCP films were then selectively metallized for the fabrication of plasmonic nanoparticle alignments by the LPI process.[38,39] As the nitrogen in the pyridine moiety of P2VP can be protonated under acidic conditions with a partial positive charge, metal ions with a negative charge (e.g., $[AuCl_4]^-$) can infiltrate the films and selectively reside in the P2VP domains through electrostatic interactions. We immersed the BCP film on the wrinkled PDMS substrate in 0.02 M of $HAuCl_4$ and 1.6 wt % HCl aqueous solution for 2 h to ensure sufficient infiltration. Then, oxygen plasma was used to etch the BCP template and reduce the gold ions to metallic gold nanoparticles. After reduction, the transferred area was changed to reddish-purple
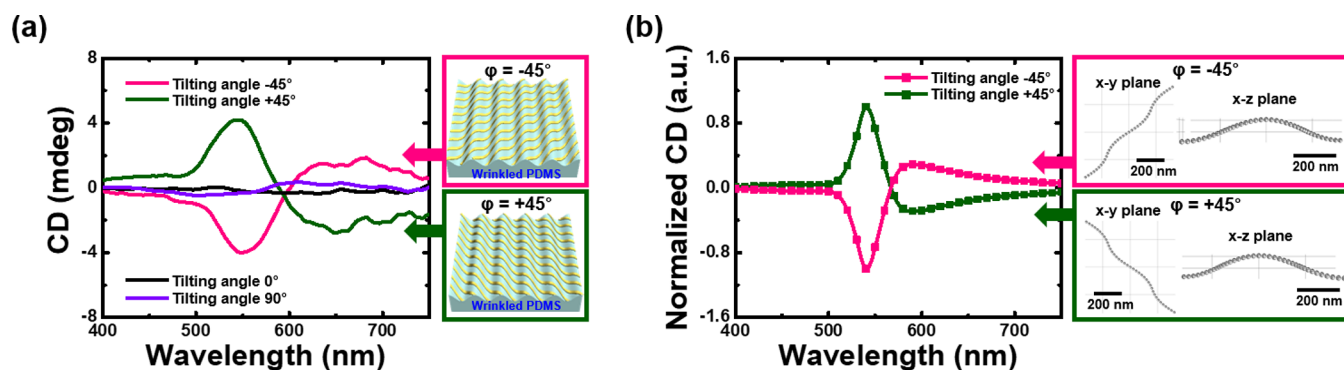
Figure 5. (a) CD spectra of chiral nanowave nanopatterns with various tilt angles of 0°, +45°, −45°, and 90°. (b) Simulated CD spectra. Model geometries in the $x-y$ planes and $x-z$ planes are shown on the right.
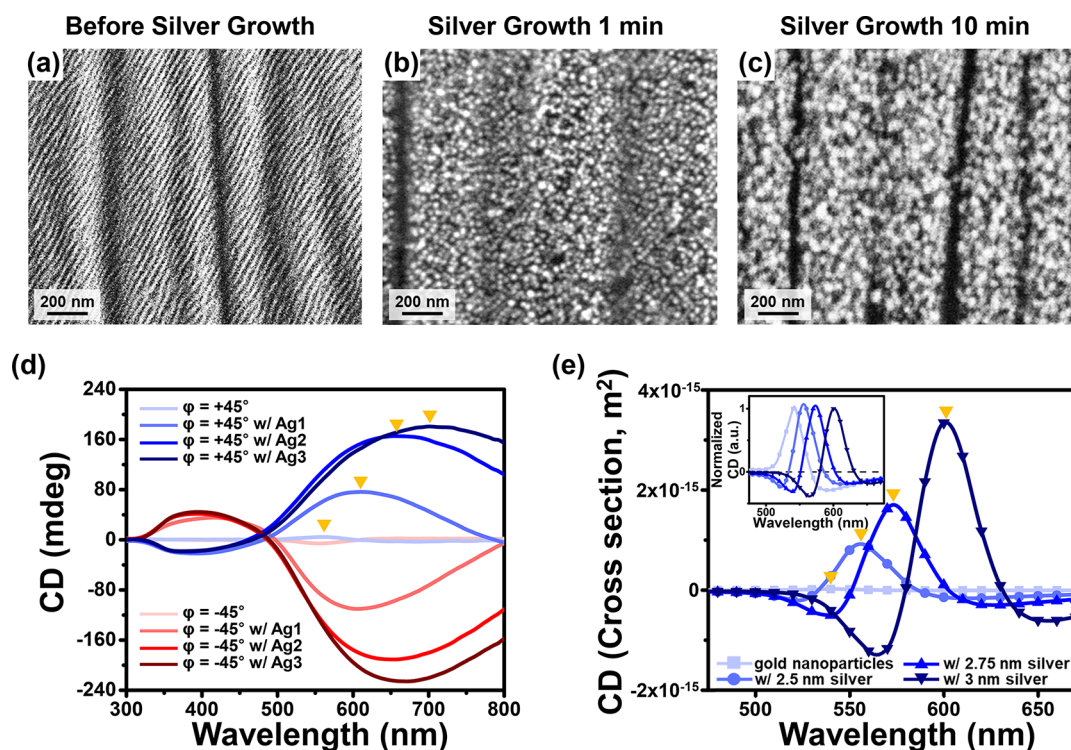

Figure 6. FE-SEM images of the chiral plasmonic nanowave patterns with $\varphi = -45°$ (a) before silver growth, (b) silver growth in 1 min, and (c) silver growth in 10 min. (d) CD spectra with the repetitive silver depositions. Inverted triangles indicate locations of maximum CD peaks. (e) Simulated CD spectra for the chiral nanoparticle chain models of $\varphi = +45°$ with 18 nm Au core and variations in Ag shells as 2, 2.5, and 3 nm.

in color and showed characteristic absorptions at ∼530 nm corresponding to plasmonic resonances from the aligned gold nanopatterns (Figure S3).

Figure 4 shows representative SEM plane images of the unidirectional plasmonic nanowave patterns on the unidirectionally wrinkled PDMS substrate fabricated with tilt angles (φ) of +45° and −45°. In both samples, at microscale observations, the microwrinkles are unidirectionally aligned with periods of ∼400 nm, indicating significant change after the metallization and etching process. Since the polymeric surface film disappears except for the metal pattern after the etching process, the wrinkle structures are mainly affected by the silicate layer of the O_2 plasma treated PDMS. Nanoscale observations confirmed that the gold nanopatterns are highly aligned with lines of ∼18 nm line-width in the tilted angles that cross over the axis of the microwrinkles. In addition, the period

of the aligned Au line pattern was greatly reduced from ∼40 nm to ∼31 nm, indicating that the nanostructure was also compressed by the compressive strain applied as the 30% prestrain was relieved. For the sample with $\varphi = +45°$, the gold nanopatterns are aligned from the upper left corner to the bottom right corner in the diagonal direction of the SEM image (Figure 4a−c). For the sample with $\varphi = -45°$, the nanopatterns run from the upper right corner to the bottom left corner (Figure 4d−f), mirroring the samples with $\varphi = +45°$. To compare with the chiral aligned nanowave patterns, gold nanowave patterns with tilt angles of 0° and 90° were also prepared; the samples showed gold nanopatterns with parallel or perpendicular alignment to the axis of the microwrinkles. (Figures S4). In addition, the period of each pattern decreased to 30.7 nm at 0° and 36.5 nm at 90° compared to the initial 40 nm, and the period contractions decreased as the angle

increased. This is because the larger is the angle of the gold line pattern with respect to the unidirectional compression (the smaller is the angle between the wrinkle direction and the gold line direction), the greater is the influence of the compression of the pattern period. With the same trend, the BCP patterns of specific angles were initially transferred to the prestrained PDMS, but after the prestrain was relieved, the angles were also changed from 45° to 33° due to unidirectional compression, as shown in Figure 3. Although the aligned gold nanopatterns are confirmed by SEM as excellent line patterns, it is known that due to the nature of the LPI process, in which metal ions are selectively attached due to electrostatic attraction, the line patterns are composed of unconnected aggregates of gold nanoparticles.[44]

The chiroptical responses of the chiral plasmonic nanowave patterns were measured using a circular dichroism (CD) spectrometer (Figure 5a). The sample with $\varphi = +45°$ shows a peak-dip shape of the CD signal with a positive maximum at ~550 nm. The sample with $\varphi = -45°$ presents a mirror-reflected CD signal relative to that observed for the sample with $\varphi = +45°$. UV−visible absorbance spectra from both samples showed similar peak positions at ~540 nm (Figure S5), which are typical plasmonic resonance absorptions from gold. Furthermore, the contribution of linear anisotropy was negligible in our experiments (Figure S6). In contrast, the control samples with $\varphi = 0°$ and 90° showed no notable CD responses even in the presence of similar plasmonic absorbances to the samples with $\varphi = +45°$ and $-45°$. On the basis of these experimental observations, nanoparticle chain models with chiral alignments were utilized to simulate the CD spectra (Figure 5b right and Figure S7). For simplicity, a single chain composed of 39 nanoparticles with diameters of 18 nm was aligned to form S-shapes representing single periodic oscillations on the microwrinkles. The simulated results show similar dip-peak CD signal shapes comparable to those observed in the experimental data (Figure 5b). Simulations of the other cases with changes of the microwrinkle periods are included in Figure S10. Overall trends in spectral shapes for the simulated CD spectra are mostly maintained, and peak positions show minor shifts in comparison to the initial model case. These results support that the simulated models are acceptable to reflect experimental results. The differences in spectral shapes between the experimental and simulated results can be attributed to the simplified conditions used in the simulations.

To improve intensities of the chiroptical responses, silver layers were additionally deposited by electroless deposition methods onto the chiral plasmonic nanowave patterns.[14,45] In the FE-SEM image of Figure 6b, the overall shapes of the nanowavy patterns were preserved at the initial stage of silver layer growth. However, further depositions resulted in overgrowth of silver layers that eventually covered all the chiral plasmonic nanopatterns. The silver layer depositions were repeated three times, and the size of the nanoparticles are measured to be around 25, 35, and 45 nm with an incremental increase along the number of depositions. (Figure 6c and Figure S8). CD measurements for the chiral nanowave patterns (Figure 6d) show increases of the peak intensities around 600−700 nm when the number of the silver depositions increases. Three repetitive depositions are enabled to enhance the CD peak intensities approximately 40−50 times. For instances, the maximum peak intensity of the chiral plasmonic nanowave patterns with $\varphi = -45°$ was -4 mdeg at 547 nm,

and it was enhanced to -226 mdeg at 671 nm. In the cases of $\varphi = +45°$ samples, only the gold sample presented 4.2 mdeg at 547 nm, and it was increased to 280.7 mdeg at 701 nm. The highest CD response has a -0.0089 g-factor (Figure S9b). Simulated CD signals were obtained for the chiral nanoparticle chains with 18 nm gold cores and 2.5, 2.75, and 3 nm thick silver shells. They show a trend that is similar to that of the experimental data (Figure 6e). The simulated spectra from the $\varphi = +45°$ geometries are selectively shown for clear comparison. Inset shows normalized CD signals to reveal relative positions of CD spectra. The enhancement and red-shift of maximum CD peaks can be attributed to increases in the absorption and scattering volumes of the chiral nanowave patterns that are accompanied by resonance coupling near the neighboring nanoparticles.

CONCLUSION

The chiral plasmonic nanowave patterns were prepared based on the directed assembly of BCP nanopatterns and their tilted transfer combined with uniaxial buckling. Unidirectional alignments at the nano- and microscale converged to yield crossed-finger-like chiral structures through the control of the tilt angles between the aligned axes of the nano- and microsized aligned patterns. To achieve large-area alignment of nanopatterns, shear-rolling was repeatedly applied to the BCP thin films under annealing conditions. The chirality of the transferred plasmonic nanowave patterns was determined by controlling the tilt angles during transfer. When the gold nanopatterns lay across the microwrinkle patterns in diagonal directions with tilt angles of $\varphi = +45°$ and $-45°$, the plasmonic nanowave patterns show active chiroptical properties. This approach is advantageous compared to conventional chiral synthesis methods because it avoids the use of biomaterials and lithographic techniques for controlling chirality. The manufacturing concept of the convergence of two different self-assembly methods could contribute to the broadening of the applicability of chiral materials for a variety of nano- and microscale structures in a hierarchical manner.

METHODS

Shear-Induced Alignment of BCP Thin Films. Aqueous solutions of 1 wt % polyvinylpyrrolidone (PVP, M_w = 1300 kg·mol^{-1}, Sigma-Aldrich) were spin-coated on a UVO-cleaned (30 min, AC-6, Ahtech LTS, Ltd.) Si wafer at 6000 rpm with a thickness of approximately 20 nm. These films were used as sacrificial layers. To fabricate the BCP thin film, 1.7 wt % polystyrene-*block*-poly(2-vinylpyridine) (PS-*b*-P2VP, 44 k−18.5 k, PolymerSource Inc.) in toluene was spin-coated on the PVP layer at 3000 rpm for ~57 nm thickness. For the unidirectional alignment of the BCP nanopatterns, a 0.8 mm-thick PDMS pad (Sylgard 184, Dow-Corning Ltd., 5:1 base:curing agent ratio, curing at 60 °C for 24 h) was conformally placed onto the BCP film, and the shear-rolling process was then performed repeatedly at 155 °C with a roller speed of 10 mm·s^{-1} and stage speed of 8 mm·s^{-1} for the sequential application of shear. Details of the shear-rolling instrument and procedure were described in our previous study.[33]

Preparation of PDMS Substrates and Tilted Transfer of BCP Thin Films. The precursor and curing agent of polydimethylsiloxane (PDMS, Sylgard 184, Dow-Corning Ltd.) were mixed (w/w: 10/1) and poured into a Petri dish, and the mixture was cured at 60 °C for 4 h in a convection oven. The cured PDMS films were mounted on the jigs of a device for prestrain application and unidirectionally stretched to approximately 30% strain. Oxygen plasma treatment (Vita, Femto Science Inc., 20 sccm, 20 mTorr) at 150 W for 10 s was applied to the prestrained PDMS films in the prestrain device. The shear-rolled BCP

films were attached to the prestrained PDMS surfaces with controlled angles (*e.g.*, 45°) between the BCP alignment direction and the prestrain direction of the PDMS substrate in the clockwise or counterclockwise direction to create chirality. After immersing the prestrained sample in deionized water at 60 °C, the PVP sacrificial layer was removed, and the BCP films were spontaneously transferred to the PDMS surfaces. Then, the applied strain was released to form unidirectional microwrinkles in the BCP/PDMS bilayer samples.

Liquid-Phase Infiltration (LPI) Process for Metallization. After the aligned BCP nanopatterns were transferred onto the PDMS substrates and buckled by the release of strains, the LPI process for selective metallization was performed by the selective infiltration of metal salt into the P2VP cylindrical nanodomains. Ar plasma treatment was performed (100 W, 20 sccm, 25 s) before the metallization, to expose cylinders of BCP nanopatterns without any cover layer to penetrate. A gold metal salt solution was prepared by dissolving 0.136 g of gold(III) chloride hydrate ($HAuCl_4 \cdot xH_2O$, 99.995%, Sigma-Aldrich) in 20 mL of 1.6 wt % aqueous hydrochloric acid solution. The BCP films on the PDMS substrates were immersed in the metal salt solution for 2 h at room temperature, and then gently rinsed several times with water. The oxygen plasma treatment was then performed (20 W, 20 sccm, 2 min) to remove the polymeric materials and reduce the metal salts. For the silver growth on nanowave patterns, commercially available silver enhancement kits (HQ Silver Enhancement, Nanoprobes, USA) were utilized. We prepared a solution for electroless deposition by mixing the components solution "A" (inhibitor), solution "B" (moderator), and solution "C" (activator) in a 1:1:1 ratio. Immediately after dropping the solutions on the PTFE plates, the samples after the LPI processes were placed upside down for 10 min. Then, the samples were rinsed gently with DI water and dried with an air gun.

Characterization. The thickness of the BCP film and PVP sacrificial layer was measured using spectral reflectometry (Filmetrics F20, USA). The microstructures of the micro- and nanopatterns were measured using field-emission scanning electron microscopy (FE-SEM, Zeiss Sigma 300, Zeiss). Before transferring the BCP film to the PDMS substrate, the alignment of the BCP nanopatterns was observed using SEM by exposing the film to iodine vapor for 4 h for selective staining of the P2VP domains. The periodicity and amplitude of the micro- and nanopatterns were acquired using atomic force microscopy (AFM, MFP-3D, Asylum Research). The chiroptical properties were measured using a circular dichroism spectrometer (J-1100, JASCO).

Simulation of CD Spectra. Chiral nanowave patterns were simulated using the finite element method (FEM) in COMSOL software. An electromagnetic module embedded with Maxwell's equations was utilized for the physics setting. Scattering fields of left- or right-handed circularly polarized light with scattering sphere models were utilized as described earlier.[22,46] Total extinctions were obtained by the summation of the absorption and scattering extinctions under each circularly polarized light, and CD spectra were obtained by the subtraction of the extinction for RCP from that for LCP. Each model of the S-shaped aligned chains was composed of 39 spherical nanoparticles with a diameter of 18 nm. The model represented a tilted array of gold nanoparticles across sinusoidal microscale wrinkles. The distances between the two nanoparticles at both ends were 637 and 653 nm in the *x* and *y* directions, respectively. The distance along the *x*-direction was adjusted to values similar to the periodicity of the microwrinkles. The highest-amplitude positions of the nanoparticles were 50 nm in a sinusoidal representation of the microwrinkle. The distance between the nanoparticles was fixed at 7 nm. The PDMS substrates were not included in the models for simplicity, and the environment was set to $n = 1.25$. Refractive indices of gold and silver were adapted from the literature.[47,48] For simulation of the silver layer overgrowth experiments, 2.5, 2.75, and 3 nm thick silver shell layers are added to gold nanoparticles.

ASSOCIATED CONTENT

ⓈⒾ Supporting Information

The Supporting Information is available free of charge at https://pubs.acs.org/doi/10.1021/acsnano.1c03752.

> Schematic illustrations of asymmetrically aligned nanowave patterns with chirality; SEM and AFM images of wrinkled nanoscale patterns of PDMS by O_2 plasma; photographs and UV−vis absorbance spectra of the samples before and after metallization; SEM images and UV−vis absorbance spectra of the plasmonic nanopatterns fabricated with tilt angles of 0° and 90°; CD measured with different azimuthal angles of rotation; images of simulated models in inclined-angle view; SEM image, UV−vis absorbance spectra, and simulation results of after silver depositions (PDF)

AUTHOR INFORMATION

Corresponding Authors

Jeong Gon Son − *Soft Hybrid Materials Research Center, Korea Institute of Science and Technology (KIST), Seongbuk-gu, Seoul 02792, Republic of Korea; KU-KIST Graduate School of Converging Science and Technology, Korea University, Seongbuk-gu, Seoul 02841, Republic of Korea;* ⓞ orcid.org/0000-0003-3473-446X; Email: jgson@kist.re.kr

Bongjun Yeom − *Department of Chemical Engineering, Hanyang University, Seongdong-gu, Seoul 04763, Republic of Korea;* ⓞ orcid.org/0000-0001-8914-0947; Email: byeom@hanyang.ac.kr

Authors

Junghyun Cho − *Soft Hybrid Materials Research Center, Korea Institute of Science and Technology (KIST), Seongbuk-gu, Seoul 02792, Republic of Korea*

Myonghoo Hwang − *Department of Chemical Engineering, Hanyang University, Seongdong-gu, Seoul 04763, Republic of Korea*

Minkyung Shin − *Soft Hybrid Materials Research Center, Korea Institute of Science and Technology (KIST), Seongbuk-gu, Seoul 02792, Republic of Korea; Department of Chemical Engineering, Hanyang University, Seongdong-gu, Seoul 04763, Republic of Korea*

Jinwoo Oh − *Soft Hybrid Materials Research Center, Korea Institute of Science and Technology (KIST), Seongbuk-gu, Seoul 02792, Republic of Korea*

Jinhan Cho − *Department of Chemical and Biological Engineering and KU-KIST Graduate School of Converging Science and Technology, Korea University, Seongbuk-gu, Seoul 02841, Republic of Korea;* ⓞ orcid.org/0000-0002-7097-5968

Complete contact information is available at:
https://pubs.acs.org/10.1021/acsnano.1c03752

Author Contributions

[#]J.C., M.H., and M.S. equally contributed.

Notes

The authors declare no competing financial interest.

REFERENCES

(1) Hwang, M.; Yeom, B. Fabrication of Chiral Materials in Nano- and Microscale. *Chem. Mater.* **2021**, *33*, 807−817.

(2) Luo, Y.; Chi, C.; Jiang, M.; Li, R.; Zu, S.; Li, Y.; Fang, Z. Plasmonic Chiral Nanostructures: Chiroptical Effects and Applications. *Adv. Opt. Mater.* **2017**, *5*, 1700040.

(3) Zhang, S.; Park, Y. S.; Li, J.; Lu, X.; Zhang, W.; Zhang, X. Negative Refractive Index in Chiral Metamaterials. *Phys. Rev. Lett.* **2009**, *102*, 023901.

(4) Mun, J.; Kim, M.; Yang, Y.; Badloe, T.; Ni, J.; Chen, Y.; Qiu, C.-W.; Rho, J. Electromagnetic Chirality: From Fundamentals to Nontraditional Chiroptical Phenomena. *Light: Sci. Appl.* **2020**, *9*, 139.

(5) Wen, D.; Yue, F.; Li, G.; Zheng, G.; Chan, K.; Chen, S.; Chen, M.; Li, K. F.; Wong, P. W. H.; Cheah, K. W.; Yue Bun Pun, E.; Zhang, S.; Chen, X. Helicity Multiplexed Broadband Metasurface Holograms. *Nat. Commun.* **2015**, *6*, 8241.

(6) Cao, T.; Qiu, Y. Lateral Sorting of Chiral Nanoparticles Using Fano-Enhanced Chiral Force in Visible Region. *Nanoscale* **2018**, *10*, 566−574.

(7) Rodríguez-Fortuño, F. J.; Engheta, N.; Martínez, A.; Zayats, A. V. Lateral Forces on Circularly Polarizable Particles near a Surface. *Nat. Commun.* **2015**, *6*, 8799.

(8) Hendry, E.; Carpy, T.; Johnston, J.; Popland, M.; Mikhaylovskiy, R. V.; Lapthorn, A. J.; Kelly, S. M.; Barron, L. D.; Gadegaard, N.; Kadodwala, M. Ultrasensitive Detection and Characterization of Biomolecules Using Superchiral Fields. *Nat. Nanotechnol.* **2010**, *5* (11), 783−787.

(9) Kakkar, T.; Keijzer, C.; Rodier, M.; Bukharova, T.; Taliansky, M.; Love, A. J.; Milner, J. J.; Karimullah, A. S.; Barron, L. D.; Gadegaard, N.; Lapthorn, A. J.; Kadodwala, M. Superchiral near Fields Detect Virus Structure. *Light: Sci. Appl.* **2020**, *9*, 2047−7538.

(10) Lee, H. E.; Ahn, H. Y.; Mun, J.; Lee, Y. Y.; Kim, M.; Cho, N. H.; Chang, K.; Kim, W. S.; Rho, J.; Nam, K. T. Amino-Acid- and Peptide-Directed Synthesis of Chiral Plasmonic Gold Nanoparticles. *Nature* **2018**, *556*, 360−364.

(11) Gao, X.; Han, B.; Yang, X.; Tang, Z. Perspective of Chiral Colloidal Semiconductor Nanocrystals: Opportunity and Challenge. *J. Am. Chem. Soc.* **2019**, *141*, 13700−13707.

(12) Hentschel, M.; Schäferling, M.; Weiss, T.; Liu, N.; Giessen, H. Three-Dimensional Chiral Plasmonic Oligomers. *Nano Lett.* **2012**, *12*, 2542−2547.

(13) Duan, X.; Yue, S.; Liu, N. Understanding Complex Chiral Plasmonics. *Nanoscale* **2015**, *7*, 17237−17243.

(14) Kuzyk, A.; Schreiber, R.; Fan, Z.; Pardatscher, G.; Roller, E.-M.; Högele, A.; Simmel, F. C.; Govorov, A. O.; Liedl, T. DNA-Based Self-Assembly of Chiral Plasmonic Nanostructures with Tailored Optical Response. *Nature* **2012**, *483*, 311−314.

(15) Zion, M. Y.; Ben; He, X.; Maass, C. C.; Sha, R.; Seeman, N. C.; Chaikin, P. M. Self-Assembled Three-Dimensional Chiral Colloidal Architecture. *Science* **2017**, *358*, 633−636.

(16) Choi, W. J.; Cheng, G.; Huang, Z.; Zhang, S.; Norris, T. B.; Kotov, N. A. Terahertz Circular Dichroism Spectroscopy of Biomaterials Enabled by Kirigami Polarization Modulators. *Nat. Mater.* **2019**, *18*, 820−826.

(17) Liu, Z.; Du, H.; Li, J.; Lu, L.; Li, Z. Y.; Fang, N. X. Nano-Kirigami with Giant Optical Chirality. *Sci. Adv.* **2018**, *4*, eaat4436.

(18) Mark, A. G.; Gibbs, J. G.; Lee, T.-C.; Fischer, P. Hybrid Nanocolloids with Programmed Three-Dimensional Shape and Material Composition. *Nat. Mater.* **2013**, *12*, 802−807.

(19) Singh, H. J.; Ghosh, A. Large and Tunable Chiro-Optical Response with All Dielectric Helical Nanomaterials. *ACS Photonics* **2018**, *5*, 1977−1985.

(20) Yeom, B.; Zhang, H.; Zhang, H.; Park, J. Il; Kim, K.; Govorov, A. O.; Kotov, N. A. Chiral Plasmonic Nanostructures on Achiral Nanopillars. *Nano Lett.* **2013**, *13*, 5277−5283.

(21) Wang, Z.; Ai, B.; Zhou, Z.; Guan, Y.; Möhwald, H.; Zhang, G. Free-Standing Plasmonic Chiral Metamaterials with 3D Resonance Cavities. *ACS Nano* **2018**, *12*, 10914−10923.

(22) Kim, Y.; Yeom, B.; Arteaga, O.; Yoo, S. J.; Lee, S. G.; Kim, J. G.; Kotov, N. A. Reconfigurable Chiroptical Nanocomposites with Chirality Transfer from the Macro- to the Nanoscale. *Nat. Mater.* **2016**, *15*, 461−468.

(23) Hwang, M.; Kim, C.; Kim, J.; Son, J. G.; Yeom, B. Controlled Fabrication of 3D Chiral Microwrinkles *via* Asymmetrical and Biaxial Bucklings. *Adv. Funct. Mater.* **2019**, *29*, 1808979.

(24) Manoccio, M.; Esposito, M.; Passaseo, A.; Cuscunà, M.; Tasco, V. Focused Ion Beam Processing for 3D Chiral Photonics Nanostructures. *Micromachines* **2021**, *12*, 6.

(25) Liu, C.-C.; Franke, E.; Mignot, Y.; Xie, R.; Yeung, C. W.; Zhang, J.; Chi, C.; Zhang, C.; Farrell, R.; Lai, K.; Tsai, H.; Felix, N.; Corliss, D. Directed Self-Assembly of Block Copolymers for 7 Nanometre FinFET Technology and Beyond. *Nat. Electron.* **2018**, *1*, 562−569.

(26) Griffiths, R. A.; Williams, A.; Oakland, C.; Roberts, J.; Vijayaraghavan, A.; Thomson, T. Directed Self-Assembly of Block Copolymers for Use in Bit Patterned Media Fabrication. *J. Phys. D: Appl. Phys.* **2013**, *46*, 503001.

(27) Stefik, M.; Guldin, S.; Vignolini, S.; Wiesner, U.; Steiner, U. Block Copolymer Self-Assembly for Nanophotonics. *Chem. Soc. Rev.* **2015**, *44*, 5076−5091.

(28) Yang, J. K. W.; Jung, Y. S.; Chang, J.-B.; Mickiewicz, R. A.; Alexander-Katz, A.; Ross, C. A.; Berggren, K. K. Complex Self-Assembled Patterns Using Sparse Commensurate Templates with Locally Varying Motifs. *Nat. Nanotechnol.* **2010**, *5*, 256−260.

(29) Kim, S. O.; Solak, H. H.; Stoykovich, M. P.; Ferrier, N. J.; De Pablo, J. J.; Nealey, P. F. Epitaxial Self-Assembly of Block Copolymers on Lithographically Defined Nanopatterned Substrates. *Nature* **2003**, *424*, 411−414.

(30) Oh, J.; Suh, H. S.; Ko, Y.; Nah, Y.; Lee, J.; Yeom, B.; Char, K.; Ross, C. A.; Son, J. G. Universal Perpendicular Orientation of Block Copolymer Microdomains Using a Filtered Plasma. *Nat. Commun.* **2019**, *10*, 2912.

(31) Angelescu, D. E.; Waller, J. H.; Adamson, D. H.; Deshpande, P.; Chou, S. Y.; Register, R. A.; Chaikin, P. M. Macroscopic Orientation of Block Copolymer Cylinders in Single-Layer Films by Shearing. *Adv. Mater.* **2004**, *16*, 1736−1740.

(32) Kim, Y. C.; Shin, T. J.; Hur, S.; Kwon, S. J.; Kim, S. Y. Shear-Solvo Defect Annihilation of Diblock Copolymer Thin Films over a Large Area. *Sci. Adv.* **2019**, *5*, eaaw3974.

(33) Oh, J.; Shin, M.; Kim, I. S.; Suh, H. S.; Kim, Y.; Kim, J. K.; Bang, J.; Yeom, B.; Son, J. G. Shear-Rolling Process for Unidirectionally and Perpendicularly Oriented Sub-10-nm Block Copolymer Patterns at the 4-Inch Scale. *ACS Nano* **2021**, *15*, 8549−8558.

(34) Kim, C.-J.; Sánchez-Castillo, A.; Ziegler, Z.; Ogawa, Y.; Noguez, C.; Park, J. Chiral Atomically Thin Films. *Nat. Nanotechnol.* **2016**, *11*, 520−524.

(35) Kuzyk, A.; Schreiber, R.; Zhang, H.; Govorov, A. O.; Liedl, T.; Liu, N. Reconfigurable 3D Plasmonic Metamolecules. *Nat. Mater.* **2014**, *13*, 862−866.

(36) Ma, W.; Kuang, H.; Wang, L.; Xu, L.; Chang, W. S.; Zhang, H.; Sun, M.; Zhu, Y.; Zhao, Y.; Liu, L.; Xu, C.; Link, S.; Kotov, N. A. Chiral Plasmonics of Self-Assembled Nanorod Dimers. *Sci. Rep.* **2013**, *3*, 1934.

(37) Probst, P. T.; Mayer, M.; Gupta, V.; Steiner, A. M.; Zhou, Z.; Auernhammer, G. K.; König, T. A.; Fery, A. Mechano-Tunable Chiral Metasurfaces *via* Colloidal Assembly. *Nat. Mater.* **2021**, *20*, 1024−1028.

(38) Chai, J.; Wang, D.; Fan, X.; Buriak, J. M. Assembly of Aligned Linear Metallic Patterns on Silicon. *Nat. Nanotechnol.* **2007**, *2*, 500−506.

(39) Subramanian, A.; Tiwale, N.; Doerk, G.; Kisslinger, K.; Nam, C. Y. Enhanced Hybridization and Nanopatterning *via* Heated Liquid-Phase Infiltration into Self-Assembled Block Copolymer Thin Films. *ACS Appl. Mater. Interfaces* **2020**, *12*, 1444−1453.

(40) Lee, S.-H.; Kang, H.; Cho, J.; Kim, Y. S.; Char, K. Dual Morphology of Islands and Fractal Holes in Block Copolymer Thin Films. *Macromolecules* **2001**, *34*, 8405−8408.

(41) Kim, Y. C.; Kim, S. Y. Fabrication of Gold Nanowires in Micropatterns Using Block Copolymers. *RSC Adv.* **2018**, *8*, 19532−19538.

(42) Zhang, L.; Cui, T.; Cao, X.; Zhao, C.; Chen, Q.; Wu, L.; Li, H. Inorganic-Macroion-Induced Formation of Bicontinuous Block Copolymer Nanocomposites with Enhanced Conductivity and Modulus. *Angew. Chem., Int. Ed.* **2017**, *56*, 9013−9017.

(43) Chen, C. M.; Yang, S. Wrinkling Instabilities in Polymer Films and Their Applications. *Polym. Int.* **2012**, *61*, 1041−1047.

(44) Lee, W.; Lee, S.; Tang, A. S.; Kim, C.; Liu, R.; Im, K.; Jung, H.-T.; Ross, C. A. Platinum Infiltration of a Block Copolymer for Interconnected Three-Dimensional Metal Nanostructures. *ACS Appl. Nano Mater.* **2021**, *4*, 793−801.

(45) Tremi, I.; Havaki, S.; Georgitsopoulou, S.; Lagopati, N.; Georgakilas, V.; Gorgoulis, V. G.; Georgakilas, A. G. A Guide for Using Transmission Electron Microscopy for Studying the Radio-sensitizing Effects of Gold Nanoparticles *in Vitro*. *Nanomaterials* **2021**, *11*, 859.

(46) Jung, A.; Kim, C.; Yeom, B. Birefringence-Induced Modulation of Optical Activity in Chiral Plasmonic Helical Arrays. *J. Phys. Chem. Lett.* **2017**, *8*, 1872−1877.

(47) Johnson, P. B.; Christy, R. W. Optical Constants of the Noble Metals. *Phys. Rev. B* **1972**, *6*, 4370−4379.

(48) Werner, W. S.; Glantschnig, K.; Ambrosch-Draxl, C. Optical Constants and Inelastic Electron-Scattering Data for 17 Elemental Metals. *J. Phys. Chem. Ref. Data* **2009**, *38*, 1013−1092.